



ARL-TR-8736 • JULY 2019



Growth and Characterization of Graphene/ Bismuth Telluride Heterostructures

by Travis M Tumlin, Lily Giri, Mark H Griep, and Shashi P Karna

Approved for public release; distribution is unlimited.

NOTICES

Disclaimers

The findings in this report are not to be construed as an official Department of the Army position unless so designated by other authorized documents.

Citation of manufacturer's or trade names does not constitute an official endorsement or approval of the use thereof.

Destroy this report when it is no longer needed. Do not return it to the originator.



Growth and Characterization of Graphene/ Bismuth Telluride Heterostructures

by Travis M Tumlin and Lily Giri

Oak Ridge Institute for Science and Education (ORISE)

Mark H Griep and Shashi P Karna

Weapons and Materials Research Directorate, CCDC Army Research Laboratory

REPORT DOCUMENTATION PAGE				Form Approved OMB No. 0704-0188	
<p>Public reporting burden for this collection of information is estimated to average 1 hour per response, including the time for reviewing instructions, searching existing data sources, gathering and maintaining the data needed, and completing and reviewing the collection information. Send comments regarding this burden estimate or any other aspect of this collection of information, including suggestions for reducing the burden, to Department of Defense, Washington Headquarters Services, Directorate for Information Operations and Reports (0704-0188), 1215 Jefferson Davis Highway, Suite 1204, Arlington, VA 22202-4302. Respondents should be aware that notwithstanding any other provision of law, no person shall be subject to any penalty for failing to comply with a collection of information if it does not display a currently valid OMB control number.</p> <p>PLEASE DO NOT RETURN YOUR FORM TO THE ABOVE ADDRESS.</p>					
1. REPORT DATE (DD-MM-YYYY) July 2019		2. REPORT TYPE Technical Report		3. DATES COVERED (From - To) June 2014–September 2015	
4. TITLE AND SUBTITLE Growth and Characterization of Graphene/Bismuth Telluride Heterostructures				5a. CONTRACT NUMBER	
				5b. GRANT NUMBER	
				5c. PROGRAM ELEMENT NUMBER	
6. AUTHOR(S) Travis M Tumlin, Lily Giri, Mark H Griep, and Shashi P Karna				5d. PROJECT NUMBER	
				5e. TASK NUMBER	
				5f. WORK UNIT NUMBER	
7. PERFORMING ORGANIZATION NAME(S) AND ADDRESS(ES) CCDC Army Research Laboratory ATTN: FCDD-RLW-MG Aberdeen Proving Ground, MD 21005-5066				8. PERFORMING ORGANIZATION REPORT NUMBER ARL-TR-8736	
9. SPONSORING/MONITORING AGENCY NAME(S) AND ADDRESS(ES)				10. SPONSOR/MONITOR'S ACRONYM(S)	
				11. SPONSOR/MONITOR'S REPORT NUMBER(S)	
12. DISTRIBUTION/AVAILABILITY STATEMENT Approved for public release; distribution is unlimited.					
13. SUPPLEMENTARY NOTES ORCID ID(s): Griep, 0000-0001-6460-8304					
14. ABSTRACT <p>Graphene (G)-based van der Waals heterostructures have recently attracted substantial attention due to the degree of customization afforded with these systems along with the ability to overcome drawbacks associated with their single-layer counterparts. The integration of ultra-high-mobility graphene with other 2-D materials provides an excellent approach for harnessing graphene's extraordinary electronic properties while allowing for greater complexity and control in switching and energy-harvesting devices. The quality, design, and controlled fabrication of these heterostructures rely on a detailed understanding of the growth mechanisms and transfer techniques. Here we present assembly and characterization of bi- and trilayer G/Bi₂Te₃/G heterostructures via a combination of transfer and chemical vapor deposition growth techniques. The fabrication of bilayer G/Bi₂Te₃ was accomplished through epitaxial growth of bismuth telluride nanoplates directly on graphene. The graphene third layer was then deposited using a polymer-assisted transfer technique to create trilayer G/Bi₂Te₃/G sandwich structures. Electrical measurements of the assembled heterostructure demonstrated an increase in sheet resistance with the growth of Bi₂Te₃ on graphene. The sheet resistance further decreases with the addition of a top graphene layer below the value of pristine graphene monolayer, suggesting that Bi₂Te₃ plays an important role in the surface sensitive mobility of electrons across graphene.</p>					
15. SUBJECT TERMS graphene, bismuth telluride, heterostructures, nanoelectronics, multifunctional devices					
16. SECURITY CLASSIFICATION OF:			17. LIMITATION OF ABSTRACT UU	18. NUMBER OF PAGES 24	19a. NAME OF RESPONSIBLE PERSON Mark Griep
a. REPORT Unclassified	b. ABSTRACT Unclassified	c. THIS PAGE Unclassified			19b. TELEPHONE NUMBER (Include area code) 410-306-4953

Contents

List of Figures	iv
1. Introduction	1
2. Experimental Procedure	2
2.1 Graphene Synthesis and Transfer	2
2.2 Bismuth Telluride Growth	2
2.3 Graphene/Bismuth Telluride Heterostructure Fabrication	3
2.4 Characterization	3
3. Results	4
4. Conclusion	10
5. References	11
List of Symbols, Abbreviations, and Acronyms	17
Distribution List	18

List of Figures

Fig. 1	Transfer of graphene(G)/bismuth telluride(Bi_2Te_3)/graphene(G) from silicon growth wafer to TEM grid using cellulose acetate	3
Fig. 2	Characterization of $\text{G}/\text{Bi}_2\text{Te}_3/\text{G}$ heterostructures: a) Difference in optical contrast for each structure on SiO_2/Si . b) Sheet resistance of monolayer graphene compared to $\text{G}/\text{Bi}_2\text{Te}_3$ and $\text{G}/\text{Bi}_2\text{Te}_3/\text{G}$ heterostructures. The connecting lines between data points are intended as a guide for the eye. c) Raman spectrum for various stacking orders.	5
Fig. 3	Optical micrographs of Bi_2Te_3 deposited on dendritic graphene domains. (a,c) Show graphene domains prior to Bi_2Te_3 growth. (b,d) Show the same areas in (a,c) after Bi_2Te_3 growth. Magnification for (a,b) is at $20\times$ and $100\times$ for (c,d).	6
Fig. 4	a) TEM image of a Bi_2Te_3 triangular nanoplate, b) HRTEM of Bi_2Te_3 showing lattice fringes and SAED pattern, c) thickness calculation by EELS, and d) EDS spectrum.....	7
Fig. 5	Characterization of $\text{G}/\text{Bi}_2\text{Te}_3$ heterostructures: a) Optical micrograph of $\text{G}/\text{Bi}_2\text{Te}_3$ transferred onto 285-nm SiO_2/Si . b) SEM of $\text{G}/\text{Bi}_2\text{Te}_3$ and $\text{G}/\text{Bi}_2\text{Te}_3/\text{G}$ heterostructures separated by a thick dark line running through the middle of the image. c) Magnified image of $\text{G}/\text{Bi}_2\text{Te}_3$ bilayer. d) SEM of $\text{G}/\text{Bi}_2\text{Te}_3/\text{G}$ trilayer heterostructure with prominent wrinkles (bright lines) in the top layer graphene.	8
Fig. 6	a) TEM image of $\text{G}/\text{Bi}_2\text{Te}_3$ heterostructure, b) corresponding SAED pattern, c) dark field STEM image of bilayer $\text{G}/\text{Bi}_2\text{Te}_3$ heterostructure, and d) dark field STEM image of trilayer $\text{G}/\text{Bi}_2\text{Te}_3/\text{G}$ heterostructure.....	9

1. Introduction

Graphene has been a focus of intense research in recent years due to its extraordinary electrical, mechanical, and thermal properties.¹ Ultra-high-electron mobility (up to $200,000 \text{ cm}^2\text{V}^{-1}\text{S}^{-1}$), mechanical strength (1 TPa), thermal conductivity (up to $5.3 \times 10^3 \text{ W/mK}$), and broadband energy absorption make graphene an ideal candidate for next-generation switching and energy harvesting devices.^{2–8} One major shortcoming of pristine graphene is its inherent lack of band gap.^{9,10} This lack of electronic switching (on/off) ability severely limits the electrical applications for graphene in logic devices. Various attempts to engineer a bandgap have focused on the doping of graphene, construction of bilayer graphene, and fabrication of graphene nanoribbons.^{11–13} However, these techniques have their own shortcomings, including degradation of pristine graphene resulting in decreased electron mobility, difficulty in orienting bilayer graphene, and arduous fabrication techniques with repeatability. An alternative to these methods involves the layering of graphene with bandgap-enabled materials such as hexagonal boron nitride (hBN) and transition metal dichalcogenides (TMDs).^{14–18} These techniques are advantageous in that most of these structures can be synthesized through epitaxial growth or through nondestructive layering.^{19–21} A recent advance in graphene-based van der Waals heterostructures is the epitaxial growth of topological insulators (TIs) directly onto graphene.^{22,23} TIs provide an interesting avenue for heterostructure devices due to their unique surface conducting state.^{24,25} Bismuth telluride (Bi_2Te_3) is a particularly promising candidate for graphene heterostructures owing to its similar hexagonal symmetry and small bandgap.^{26,27} Photodetector devices based on the epitaxial growth of few-layer bismuth telluride nanoplates on graphene have already been shown to outperform similar devices with other insulating materials.^{28,29} The outstanding performance of these two-layer devices has opened up the possibility for three-layer devices where bismuth telluride is sandwiched between two graphene layers. Devices based on three-layer materials have already been realized for graphene/hBN/graphene and graphene/TMD/graphene systems.^{30–39} To date, however, three-layer graphene/ Bi_2Te_3 /graphene systems have yet to be realized.

In the present work, three-layer graphene/ Bi_2Te_3 /graphene heterostructures were fabricated using a combination of epitaxial growth and polymer-assisted transfer. Bi_2Te_3 nanoplates show typical hexagonal and triangular shapes with varying thicknesses owing to the van der Waals interactions between the hexagonal unit cell of bismuth telluride and that of graphene. The similarity in the two lattices allows for the epitaxial growth of Bi_2Te_3 nanoplates on graphene with a seamless interface that promotes effective transfer and separation of carriers. The stacking of

an additional graphene layer is made possible through the use of a polymer-assisted transfer. In-plane sheet resistance shows an increase with the addition of Bi_2Te_3 over monolayer graphene while the resistance is significantly reduced with the stacking of an additional graphene monolayer. A somewhat insulating nature of bismuth telluride, despite its surface-conducting states, makes it a potential alternative for graphene devices in contrast with other insulating layers such as silicon dioxide (SiO_2) or hBN. The present work opens up avenues for future fabrication of graphene-based van der Waals structures for multiple applications.

2. Experimental Procedure

2.1 Graphene Synthesis and Transfer

Graphene was synthesized in a standard chemical vapor deposition (CVD) setup. Prior to deposition, copper foils were electropolished to remove surface impurities and reduce surface roughness. After polishing, copper foils were loaded into a 1-inch quartz tube furnace and evacuated. Hydrogen was then introduced into the system at a pressure of 350 mtorr. Samples were then rapidly heated to 1060 °C and annealed for 30 min in a hydrogen environment. For full-coverage graphene, methane was then introduced into the system at a pressure of 500 mtorr for 20 min. Subsequently, samples were rapidly cooled to room temperature and removed. A polymer-assisted method was used for graphene transfer. Briefly, 1 wt% poly(bisphenol A) carbonate in chloroform was spin coated on a graphene/copper foil sample. Samples were then floated on top of a 0.1-M solution of ammonium persulfate for approximately 2 h until no copper was visible. After which, samples were then rinsed three times in a distilled deionized water bath. Samples were then transferred to the target substrate and allowed to dry in air. Lastly, the adhering polymer was removed by rinsing the sample with chloroform and blow drying with nitrogen.

2.2 Bismuth Telluride Growth

Bismuth telluride was grown directly onto graphene via a vapor transport process. In a typical experiment, silicon or Si/SiO₂ substrates with graphene were placed inside a 1-inch quartz tube. A ceramic boat filled with 0.2 mg of bismuth telluride precursor was then placed in the center of the hot zone 9 cm away from the substrates. The tube was then evacuated and flushed three times to remove excess moisture from the system. Then, 500 sccm of argon was introduced with a pressure of 4.43 torr. The furnace was then heated to 460 °C and held at temperature for 20 min. After which, the furnace was shut down and allowed to cool naturally.

2.3 Graphene/Bismuth Telluride Heterostructure Fabrication

Heterostructures were made by taking samples with graphene already transferred onto target substrates and loading into the CVD chamber. A typical growth method was then used to deposit bismuth telluride on graphene. Additional layers of graphene were transferred on top of the bismuth telluride using polymer-assisted transfer.

For nondestructive transfer of the heterostructure sample, the replication method was used.⁴⁰ In this method, shown in Fig. 1, a negative replica of the heterostructure film surface was made with cellulose acetate film. Several drops of acetone were placed and spread on the heterostructure sample. Before allowing the acetone to evaporate, the acetate film was placed on one end of the sample and allowed to adhere to the surface via surface tension to prevent the formation of trapped air pockets. Once dry, the acetate film/heterostructure layers were carefully removed from the substrate by pulling from the edge of the film with tweezers. Next, a 4 mm² area of the acetate film/heterostructure negative replica film was cut and carefully placed, heterostructure side down, on transmission electron microscope (TEM) grids. The grids were then placed on a wetted Cu wire mesh in a petri dish. To dissolve the acetate film, acetone was added to the dish and covered with parafilm to prevent evaporation. Acetate film was completely removed after an hour, leaving the heterostructure sample on the TEM grid.

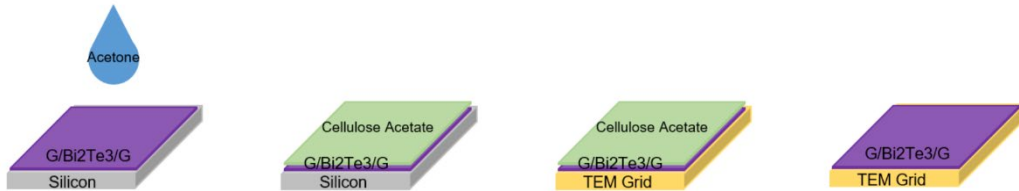


Fig. 1 Transfer of graphene(G)/bismuth telluride(Bi₂Te₃)/graphene(G) from silicon growth wafer to TEM grid using cellulose acetate

2.4 Characterization

Optical, laser, and scanning electron microscopy (SEM) were used to determine graphene coverage as well as bismuth telluride domain size and morphology. Raman spectroscopy was used to determine graphene quality throughout the transfer and deposition process. Sheet resistance measurements were performed to see the effect of heterostructure buildup on electronic properties. TEM was used to determine bismuth telluride crystal structure, thickness, and composition. The morphology of the products was analyzed using a Hitachi S4700 field emission scanning electron microscope (FESEM) equipped with an energy-dispersive X-ray system (EDS) used for average compositional analysis. TEM, high-resolution TEM

(HRTEM), and selected area electron diffraction (SAED) of the nanostructures were observed on a JEOL JEM 2100F microscope at 200 kV using an Orius SC1000 camera. Raman spectra for samples were recorded with a Horiba Jobin Yvon LabRam Aramis spectrometer at room temperature using a 532-nm excitation laser wavelength. The scattered light was analyzed with a spectrometer equipped with a detector. Both Raman and EDS results consist of an average of five measurements done at different locations on the samples. Sheet resistance of heterostructures was measured at 10 different locations on the sample using a Signatone S-302-4 in-line probe coupled with a Keithley 6430 SourceMeter.

3. Results

The as-grown G/Bi₂Te₃ heterostructures were imaged and identified by their optical contrast using optical microscopy. Figure 2a shows the optical image of G/Bi₂Te₃ heterostructures on 285-nm-thick SiO₂/Si substrates, with the synthesized nanoplates exhibiting characteristic triangular, hexagonal, and truncated triangular shapes with lateral sizes ranging from a few hundred nanometers up to several microns. The optical contrast between different nanoplates suggests a difference in quintuple layer (QL) thickness.⁴⁰ Nanoplates that appear bright white are composed of at least 20 QLs while the less contrasted plates have fewer layers. It is worth noting that individual nanoplates have uniform thickness along the entire plane. Additional synthesis experiments on nucleated graphene domains suggest inhibited growth of Bi₂Te₃ nanoplates on adlayer graphene as well as preferential growth on graphene edges, as shown in Fig. 3. This could be due to defects and dangling bonds present on graphene edges that are not found on the interior.^{41–43}

Figure 2c shows the Raman spectra of the bismuth telluride nanoplates synthesized on graphene. The presence of Bi₂Te₃ is confirmed by the characteristic E_g² and A_{1g}² Raman peaks at 102 cm⁻¹ and 132 cm⁻¹, respectively. The G and 2D peaks along with a lack of the so-called defect peak indicate the presence of pristine graphene in the graphene/Bi₂Te₃ heterostructures. A measured sheet resistance of 158±36 Ω/square, in good agreement with recently reported literature,^{44–47} also verifies the high quality of the CVD synthesized graphene. Figure 2b shows the change in sheet resistance for the heterostructure samples. The G/Bi₂Te₃ sample showed an increase in sheet resistance to 270±44 Ω/square compared to the single-layer graphene while the three-layer G/Bi₂Te₃/G showed a decrease in resistance with a value of 102±6 Ω/square, which is lower than that of single-layer graphene. The possibilities for this phenomena are discussed later in the report.

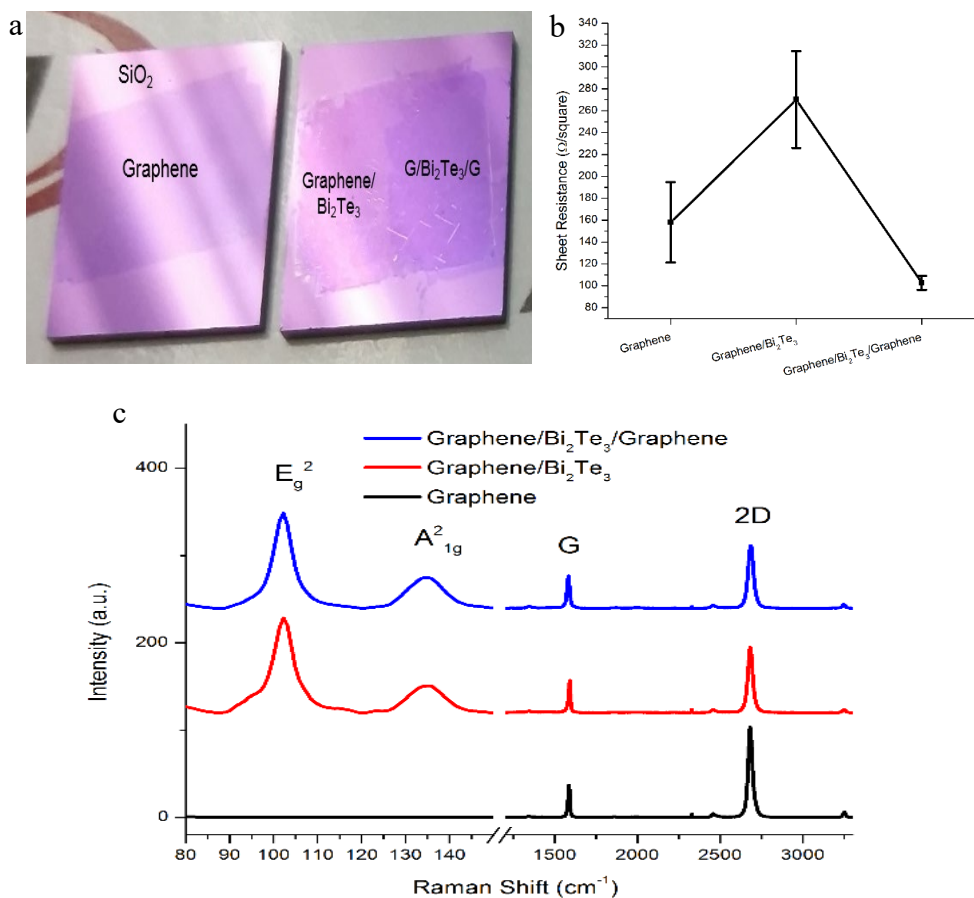


Fig. 2 Characterization of G/Bi₂Te₃/G heterostructures: a) Difference in optical contrast for each structure on SiO₂/Si. b) Sheet resistance of monolayer graphene compared to G/Bi₂Te₃ and G/Bi₂Te₃/G heterostructures. The connecting lines between data points are intended as a guide for the eye. c) Raman spectrum for various stacking orders.

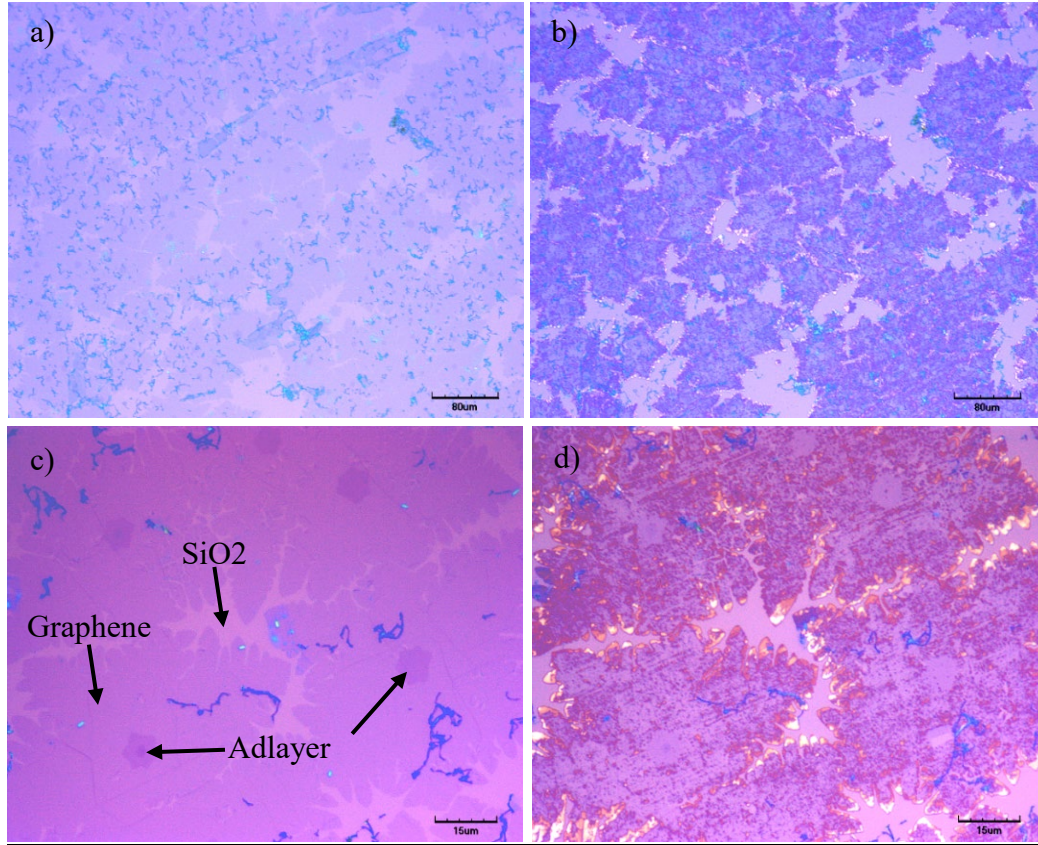


Fig. 3 Optical micrographs of Bi_2Te_3 deposited on dendritic graphene domains. (a,c) Show graphene domains prior to Bi_2Te_3 growth. (b,d) Show the same areas in (a,c) after Bi_2Te_3 growth. Magnification for (a,b) is at $20\times$ and $100\times$ for (c,d).

The crystal structure and chemical composition of the as-synthesized Bi_2Te_3 was further studied using TEM. The samples were mechanically transferred from the Si wafer to the TEM grid using 0.1-M polymethyl methacrylate in acetone. Figure 4a shows a regular TEM image of a single triangular nanoplate. High-resolution TEM in Fig. 4b shows expected hexagonal lattice fringes with a lattice spacing of 0.22 nm corresponding to (110) plane. The corresponding SAED pattern exhibits a sixfold symmetry, which confirms the single crystalline nature of the Bi_2Te_3 nanoplate. The d spacing (0.22 nm) calculated from the diffraction spots conclusively proves that those are due to diffraction from (110) plane of Bi_2Te_3 (R3m) phase. The thickness of a single hexagonal nanoplate was calculated by electron energy loss spectroscopy (EELS) and shown in Fig. 4c. The thickness profile calculated along the rectangular section in Fig. 4c was approximately 15 nm, which corresponds to approximately 15 QLs. The EDS spectrum shown in Fig. 4d gives information about the elements present as well as the composition of the nanoplates. The presence of only Bi and Te suggests that the vapor transport-deposited nanoplates are highly pure. The Cu and the C lines are coming from the

TEM grid and the holey carbon support film. Compositional analysis confirms the composition of the nanoplates with a Bi:Te atomic ratio of 2:3, indicating the Bi_2Te_3 phase.

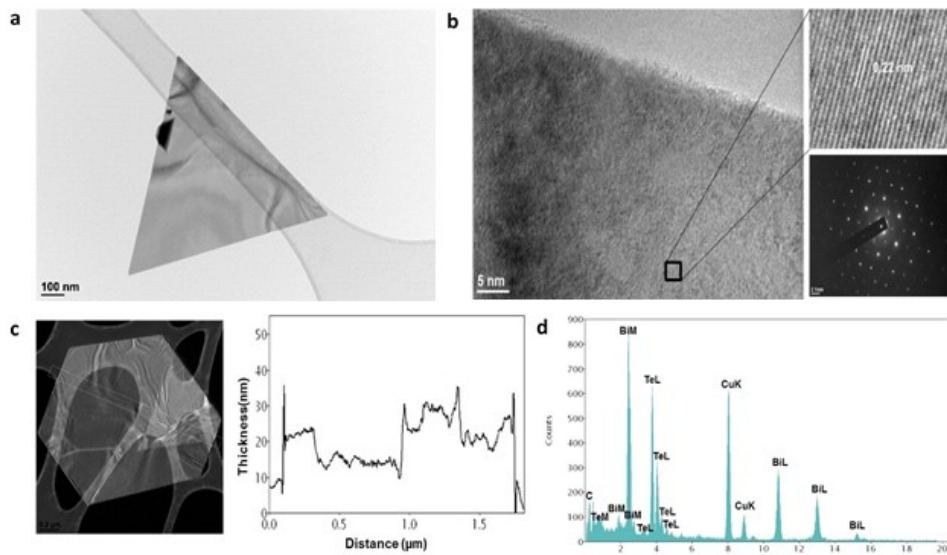


Fig. 4 a) TEM image of a Bi_2Te_3 triangular nanoplate, b) HRTEM of Bi_2Te_3 showing lattice fringes and SAED pattern, c) thickness calculation by EELS, and d) EDS spectrum

Three-layer heterostructures were fabricated using well-established polymer-assisted graphene transfer techniques.^{48–50} Figure 5a shows the contrast difference between two types of nanostructures on SiO_2/Si : $\text{G}/\text{Bi}_2\text{Te}_3$, and $\text{G}/\text{Bi}_2\text{Te}_3/\text{G}$. SEM in Fig. 5b shows the two-layer $\text{G}/\text{Bi}_2\text{Te}_3$ compared with the three-layer $\text{G}/\text{Bi}_2\text{Te}_3/\text{G}$ heterostructure. Folds and wrinkles in the images suggest the presence of a thin graphene membrane covering the Bi_2Te_3 nanoplates. The SEM images of Bi_2Te_3 nanoplates on graphene and graphene/ Bi_2Te_3 /graphene are shown in Fig. 5c and d, respectively. Figure 5c shows a clear contrast between the bare Si and the graphene with regular-shaped Bi_2Te_3 nanoplates. The SEM image of the graphene/ Bi_2Te_3 /graphene heterostructure (Fig. 5d) clearly shows folds and wrinkles of a second graphene layer on top of the Bi_2Te_3 nanoplates. This is commonly observed in large-area CVD growth of graphene on metals due to the difference in the thermal expansion coefficients of the two dissimilar systems.^{51–54} The presence of wrinkles confirms the formation of the $\text{G}/\text{Bi}_2\text{Te}_3/\text{G}$ heterostructure.

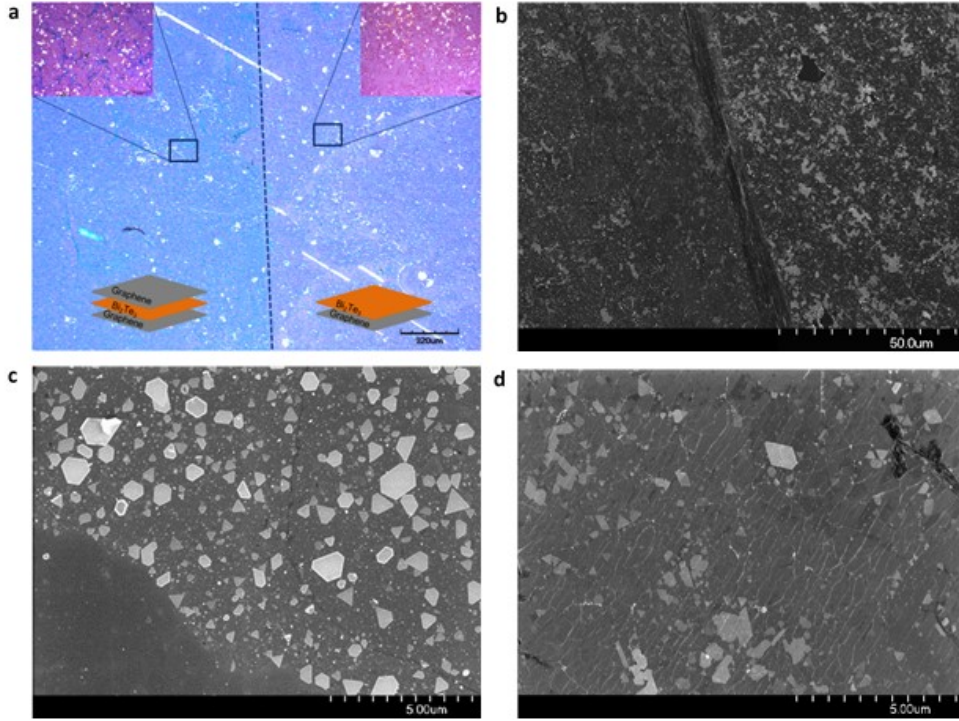


Fig. 5 Characterization of G/Bi₂Te₃ heterostructures: a) Optical micrograph of G/Bi₂Te₃ transferred onto 285-nm SiO₂/Si. b) SEM of G/Bi₂Te₃ and G/Bi₂Te₃/G heterostructures separated by a thick dark line running through the middle of the image. c) Magnified image of G/Bi₂Te₃ bilayer. d) SEM of G/Bi₂Te₃/G trilayer heterostructure with prominent wrinkles (bright lines) in the top layer graphene.

The microstructure and the composition of the heterostructures were further investigated using TEM. To prevent wrinkling, a replication transfer method was used for TEM sample preparation. Figure 6a shows the regular TEM image of the Bi₂Te₃ nanoplates grown on graphene. Randomly oriented hexagonal and triangular shaped particles can be clearly seen on the graphene film supported by the holey carbon film of the TEM grid. The particles, with lateral sizes varying from a couple hundred nanometers to several microns, are observed only on the graphene film, implying the preferential growth of Bi₂Te₃ on graphene. The SAED pattern was taken from a random area of the sample and shown in Fig. 6b. The pattern reveals hexagonal symmetry from the Bi₂Te₃ as well as that of graphene. The d spacings were calculated by rotational average method and agree very well with graphene (0.35 nm) and (110) plane spacing of Bi₂Te₃ (0.22 nm), implying the presence of pristine-quality graphene and highly pure single crystalline Bi₂Te₃.

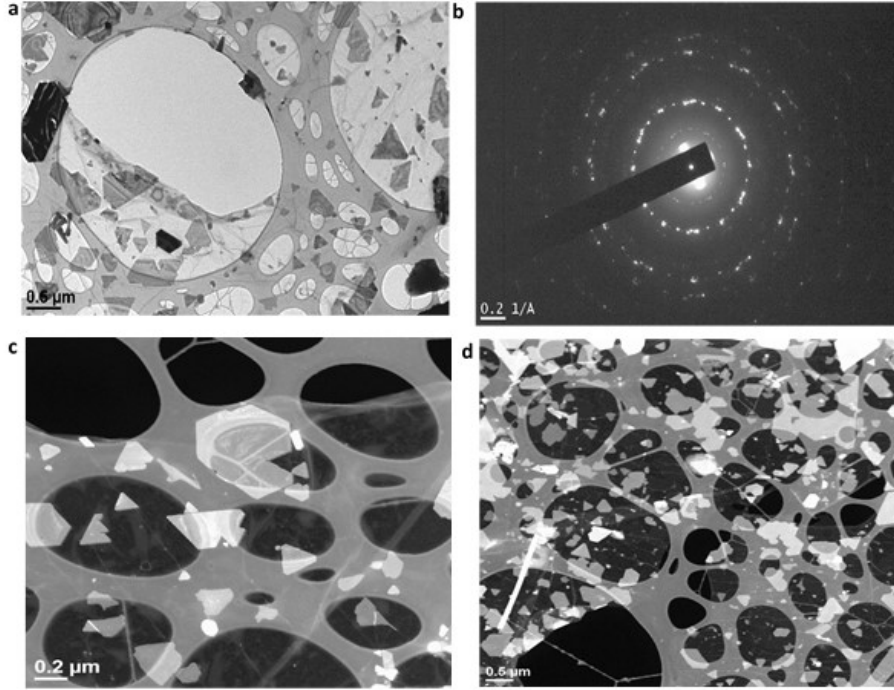


Fig. 6 a) TEM image of G/Bi₂Te₃ heterostructure, b) corresponding SAED pattern, c) dark field STEM image of bilayer G/Bi₂Te₃ heterostructure, and d) dark field STEM image of trilayer G/Bi₂Te₃/G heterostructure

For higher-contrast imaging, scanning transmission electron microscopy (STEM) was used to further observe the Bi₂Te₃ nanoplates on graphene. In the dark field image obtained by this method, the intensity varies with both the atomic number and the thickness of the material so that higher atomic number and thicker material will appear brighter. As observed from the Fig. 6c, the contrast between the bright Bi₂Te₃ nanoplates grown on graphene film and the holey carbon films is very prominent and more clearly visible. The STEM image of trilayer G/Bi₂Te₃/G (Fig. 6d) clearly shows folds and the wrinkles, which arise from the presence of a top graphene layer on Bi₂Te₃ nanoplates.

The sheet resistance, measured at room temperature, of the monolayer graphene and the G/Bi₂Te₃ and G/Bi₂Te₃/G heterostructures, shown in Fig. 2b, exhibits an interesting trend, which can be used as a useful guide to further tailor the electronic properties of G/Bi₂Te₃ heterostructures. The sheet resistance of monolayer graphene is measured to be approximately 150 Ω/square, which compares well with the previously reported values.^{55–57} The sheet resistance of the G/Bi₂Te₃ is much higher than the monolayer graphene, which is understandable, since the latter has a much lower conductivity than graphene. However, the addition of another graphene monolayer on top of the bilayer G/Bi₂Te₃ considerably reduces the sheet resistance of the top G layer. In fact, the measured value for the top G layer in the trilayer

G/Bi₂Te₃/G heterostructure is even lower than the pristine graphene monolayer. This considerable reduction in sheet resistance of G in the trilayer G/Bi₂Te₃/G could potentially result from (a) reduced surface defects/scattering centers on the second graphene layer compared to the single layer graphene,⁵⁸ (b) enhanced density of states due to coupling between the Bi₂Te₃ surface states and graphene states at the Fermi level, and/or (c) inter-layer coupling between the states of the two graphene monolayers. Enhanced density of states in bilayer graphene compared to a single monolayer, observed experimentally and predicted by density functional theory calculations, have been shown to lead to reduced resistivity.^{59,60} This could very well be the case in the present study, since Bi₂Te₃ nanostructures are not uniformly deposited on the bottom graphene surface, allowing graphene-graphene coupling in the regions lacking Bi₂Te₃ structures. Thus, mechanism (a) and (c) appear to be more plausible, although we cannot rule out the coupling between Bi₂Te₃ surface states and the top graphene states. Further experiments are underway to understand the underlying mechanism, including the role of trace amounts of polymer residues and other impurities and humidity on electronic properties of G/Bi₂Te₃. Van der Waals heterostructures will be reported in subsequent communications.

4. Conclusion

In this work, graphene/Bi₂Te₃ heterostructures were fabricated through a vapor deposition and polymer-assisted transfer process. Epitaxial growth of Bi₂Te₃ on graphene showed well-ordered nanoplates with lateral dimensions of up to approximately 10 μm and thicknesses on the order of several to tens of nanometers. Diffraction and Raman studies confirmed the high quality and crystallinity of the stacked heterostructures. Electrical characterizations show an increase and subsequent decrease in sheet resistance in going from a pristine graphene monolayer to bilayer G/Bi₂Te₃ to trilayer G/Bi₂Te₃/G heterostructures, suggesting a prominent role of Bi₂Te₃ in modulating electronic property of G-based van der Waals solids. Although the actual mechanism for the observed trend in the electrical property of the heterostructures is not clearly understood, this work provides a basis for further tailoring the electronic properties of G/Bi₂Te₃ heterostructures for useful applications.

5. References

1. Lee C, Wei X, Kysar JW, Hone J. Measurement of the elastic properties and intrinsic strength of monolayer graphene. *Science*. 2008;321(5887):385–388.
2. Mak KF, Sfeir MY, Wu Y, Lui CH, Misewich JA, Heinz TF. Measurement of the optical conductivity of graphene. *Physical Review Letters*. 2008;101(19):196405.
3. Balandin AA, Ghosh S, Bao W, Calizo I, Teweldebrhan D, Miao F, Lau CN. Superior thermal conductivity of single-layer graphene. *Nano Letters*. 2008;8(3):902–907.
4. Bolotin KI, Sikes KJ, Jiang Z, Klima M, Fudenberg G, Hone J, Stormer HL. Ultrahigh electron mobility in suspended graphene. *Solid State Communications*. 2008;46(9):351–355.
5. Wang X, Zhi L, Müllen K. Transparent, conductive graphene electrodes for dye-sensitized solar cells. *Nano Letters*. 2008;8(1):323–327.
6. Schwierz F. Graphene transistors. *Nature Nanotechnology*. 2010;5(7):487–496.
7. Ohta T, Bostwick A, Seyller T, Horn K, Rotenberg E. Controlling the electronic structure of bilayer graphene. *Science*. 2006;313(5789):951–954.
8. Novoselov KS, Geim AK, Morozov SV, Jiang D, Zhang Y, Dubonos SA, Grigorieva IV, Firsov AA. Electric field effect in atomically thin carbon films. *Science*. 2004;306(5696):666–669.
9. Novoselov KSA, Geim AK, Morozov S, Jiang D, Katsnelson M, Grigorieva I, Firsov A. Two-dimensional gas of massless Dirac fermions in graphene. *Nature*. 2005;438(7065):197–200.
10. Han MY, Özyilmaz B, Zhang Y, Kim P. Energy band-gap engineering of graphene nanoribbons. *Physical Review Letters*. 2007;98(20):206805.
11. Wei D, Liu Y, Wang Y, Zhang H, Huang L, Yu G. Synthesis of N-doped graphene by chemical vapor deposition and its electrical properties. *Nano Letters*. 2009;9(5):1752–1758.
12. Zhang Y, Tang TT, Girit C, Hao Z, Martin MC, Zettl A, Wang F. Direct observation of a widely tunable bandgap in bilayer graphene. *Nature*. 2009;459(7248):820–823.

13. Dean CR, Young AF, Meric I, Lee C, Wang L, Sorgenfrei S, Hone J. Boron nitride substrates for high-quality graphene electronics. *Nature Nanotechnology*. 2010;5(10):722–726.
14. Ci L, Song L, Jin C, Jariwala D, Wu D, Li Y, Ajayan PM. Atomic layers of hybridized boron nitride and graphene domains. *Nature Materials*. 2010;9(5):430–435.
15. Giovannetti G, Khomyakov PA, Brocks G, Kelly PJ, van den Brink J. Substrate-induced band gap in graphene on hexagonal boron nitride: ab initio density functional calculations. *Physical Review B*. 2007;76(7):073103.
16. Britnell L, Ribeiro RM, Eckmann A, Jalil R, Belle BD, Mishchenko A, Novoselov KS. Strong light-matter interactions in heterostructures of atomically thin films. *Science*. 2013;340(6138):1311–1314.
17. Bertolazzi S, Krasnozhan D, Kis A. Nonvolatile memory cells based on MoS₂/graphene heterostructures. *ACS Nano*. 2013;7(4):3246–3252.
18. Shi Y et al. Van der Waals epitaxy of MoS₂ layers using graphene as growth templates. *Nano Letters*. 2012;12(6):2784–2791.
19. Liu Z, Song L, Zhao S, Huang J, Ma L, Zhang J, Ajayan PM. Direct growth of graphene/hexagonal boron nitride stacked layers. *Nano Letters*. 2011;11(5):2032–2037.
20. Yang W, Chen G, Shi Z, Liu CC, Zhang L, Xie G, Zhang G. Epitaxial growth of single-domain graphene on hexagonal boron nitride. *Nature Materials*. 2013;12(9):792–797.
21. Dang W, Peng H, Li H, Wang P, Liu Z. Epitaxial heterostructures of ultrathin topological insulator nanoplate and graphene. *Nano Letters*. 2010;10(8):2870–2876.
22. Song CL et al. Topological insulator Bi₂Se₃ thin films grown on double-layer graphene by molecular beam epitaxy. 2010. arXiv preprint arXiv:1007.0809.
23. Zhang H, Liu CX, Qi XL, Dai X, Fang Z, Zhang SC. Topological insulators in Bi₂Se₃, Bi₂Te₃ and Sb₂Te₃ with a single Dirac cone on the surface. *Nature Physics*. 2009;5(6):438–442.
24. Qi XL, Zhang SC. The quantum spin Hall effect and topological insulators. *Physics Today*. 2010;63(1):33–38.

25. Kong D, Dang W, Cha JJ, Li H, Meister S, Peng H, Cui Y. Few-layer nanoplates of Bi_2Se_3 and Bi_2Te_3 with highly tunable chemical potential. *Nano Letters*. 2010;10(6):2245–2250.
26. Fu R, Xu S, Lu YN, Zhu JJ. Synthesis and characterization of triangular bismuth nanoplates. *Crystal Growth & Design*. 2005;5(4):1379–1385.
27. Qiao H, Yuan J, Xu Z, Chen C, Lin S, Wang Y, Bao Q. Broadband photodetectors based on graphene– Bi_2Te_3 heterostructure. *ACS Nano*. 2015;9(2):1886–1894.
28. Mu H, Wang Z, Yuan J, Xiao S, Chen C, Chen Y, Bao Q. Graphene- Bi_2Te_3 heterostructure as saturable absorber for short pulse generation. *ACS Photonics*. 2015.
29. Liu Z, Ma L, Shi G, Zhou W, Gong Y, Lei S, Ajayan PM. In-plane heterostructures of graphene and hexagonal boron nitride with controlled domain sizes. *Nature Nanotechnology*. 2013;8(2):119–124.
30. Dean CR, Young AF, Meric I, Lee C, Wang L, Sorgenfrei S, Hone J. Boron nitride substrates for high-quality graphene electronics. *Nature Nanotechnology*. 2010;5(10):722–726.
31. Xu Y, Guo Z, Chen H, Yuan Y, Lou J, Lin X, Yu B. In-plane and tunneling pressure sensors based on graphene/hexagonal boron nitride heterostructures. *Applied Physics Letters*. 2011;99(13):133109.
32. Lee GH, Yu YJ, Cui X, Petrone N, Lee CH, Choi MS, Hone J. Flexible and transparent MoS_2 field-effect transistors on hexagonal boron nitride-graphene heterostructures. *ACS Nano*. 2013;7(9):7931–7936.
33. Levendorf MP, Kim CJ, Brown L, Huang PY, Havener RW, Muller DA, Park, J. Graphene and boron nitride lateral heterostructures for atomically thin circuitry. *Nature*. 2012;488(7413):627–632.
34. Ci L, Song L, Jin C, Jariwala D, Wu D, Li Y, Ajayan PM. Atomic layers of hybridized boron nitride and graphene domains. *Nature Materials*. 2010;9(5):430–435.
35. Liu Z, Song L, Zhao S, Huang J, Ma L, Zhang J, Ajayan PM. Direct growth of graphene/hexagonal boron nitride stacked layers. *Nano Letters*. 2011;11(5):2032–2037.

36. Roy K, Padmanabhan M, Goswami S, Sai TP, Ramalingam G, Raghavan S, Ghosh A. Graphene-MoS₂ hybrid structures for multifunctional photoresponsive memory devices. *Nature Nanotechnology*. 2013;8(11):826–830.
37. Zhang W et al. Ultrahigh-gain photodetectors based on atomically thin graphene-MoS₂ heterostructures. *Scientific Reports*. 2014;4.
38. Yu L, Lee YH, Ling X, Santos EJ, Shin YC, Lin Y, Palacios T. Graphene/MoS₂ hybrid technology for large-scale two-dimensional electronics. *Nano Letters*. 2014;14(6):3055–3063.
39. Zhao Y, de la Mata M, Qiu RL, Zhang J, Wen X, Magen C, Gao XPA, Arbiol J, Xiong Q. Te-seeded growth of few-quintuple layer Bi₂Te₃ nanoplates. *Nano Research*. 2014;7(9):1243–1253.
40. Wen Q, Qian W, Nie J, Cao A, Ning G, Wang Y, Hu L, Zhang Q, Huang J, Wei F. 100 mm long, semiconducting triple-walled carbon nanotubes. *Advanced Materials*. 2010;22(16):1867–1871.
41. Casiraghi C, Hartschuh A, Qian H, Piscanec S, Georgi C, Fasoli A, Ferrari AC. Raman spectroscopy of graphene edges. *Nano Letters*. 2009;9(4):1433–1441.
42. Boukhvalov DW, Katsnelson MI. Chemical functionalization of graphene with defects. *Nano Letters*. 2008;8(12):4373–4379.
43. Koskinen P, Malola S, Häkkinen H. Self-passivating edge reconstructions of graphene. *Physical Review Letters*. 2008;101(11):115502.
44. Peng SA et al. The sheet resistance of graphene under contact and its effect on the derived specific contact resistivity. *Carbon*. 2015;82:500–505.
45. Shikoh A, Popelka A, Touati F, Benammar M, Zhu Z, Mankowski T, Falco C. Highly transparent low sheet resistance electrodes for solar cell applications. In *Microelectronics (ICM), 2014 26th International Conference on*. IEEE; 2014 Dec. pp 196–199.
46. Choi YY, Kang SJ, Kim HK, Choi WM, Na SI. Multilayer graphene films as transparent electrodes for organic photovoltaic devices. *Solar Energy Materials and Solar Cells*. 2012;96:281–285.
47. Krupka J, Strupinski W. Measurements of the sheet resistance and conductivity of thin epitaxial graphene and SiC films. *Applied Physics Letters*. 2010;96(8): 2101.

48. Zhu W, Low T, Perebeinos V, Bol AA, Zhu Y, Yan H, Avouris P. Structure and electronic transport in graphene wrinkles. *Nano Letters*. 2012;12(7):3431–3436.
49. Yan Z, Lin J, Peng Z, Sun Z, Zhu Y, Li L, Tour JM. Toward the synthesis of wafer-scale single-crystal graphene on copper foils. *ACS Nano* 2012;6(10):9110–9117.
50. Lee Y, Bae S, Jang H, Jang S, Zhu SE, Sim SH, Ahn JH. Wafer-scale synthesis and transfer of graphene films. *Nano Letters*. 2010;10(2):490–493.
51. Liang X, Sperling BA, Calizo I, Cheng G, Hacker CA, Zhang Q, Richter CA. Toward clean and crackless transfer of graphene. *ACS Nano*. 2011;5(11):9144–9153.
52. Chae SJ et al. Synthesis of large-area graphene layers on poly-nickel substrate by chemical vapor deposition: wrinkle formation. *Adv Mater*. 2009;21(22):2328–2333.
53. Zhang Y, Gao T, Gao Y, Xie S, Ji Q, Yan K, Liu Z. Defect-like structures of graphene on copper foils for strain relief investigated by high-resolution scanning tunneling microscopy. *ACS Nano*. 2011;5(5):4014–4022.
54. Paronyan TM, Pigos EM, Chen G, Harutyunyan AR. Formation of ripples in graphene as a result of interfacial instabilities. *ACS Nano*. 2011;5(12):9619–9627.
55. Lin YC, Jin C, Lee JC, Jen SF, Suenaga K, Chiu PW. Clean transfer of graphene for isolation and suspension. *ACS Nano*. 2011;5(3):2362–2368.
56. Kwak BW, Choi YC, Lee BS. Small variations in the sheet resistance of graphene layers with compressive and tensile bending. *Physica E: Low-dimensional Systems and Nanostructures*. 2015;68:33–37.
57. Bae S, Kim H, Lee Y, Xu X, Park JS, Zheng Y, Iijima S. Roll-to-roll production of 30-inch graphene films for transparent electrodes. *Nature Nanotechnology* 2010;5(8):574–578.
58. Tongay S, Berke K, Lemaitre M, Nasrollahi Z, Tanner DB, Hebard AF, Appleton BR. Stable hole doping of graphene for low electrical resistance and high optical transparency. *Nanotechnology*. 2011;22(42):425701.

59. Bao W, Jing L, Velasco Jr J, Lee Y, Liu G, Tran D, Lau CN. Stacking-dependent band gap and quantum transport in trilayer graphene. *Nature Physics*. 2011;7(12):948–952.
60. Zhong X, Pandey R, Karna SP. Stacking dependent electronic structure and transport in bilayer graphene nanoribbons. *Carbon*. 2012;50(3):784–790.

List of Symbols, Abbreviations, and Acronyms

2-D	2-dimensional
Bi ₂ Te ₃	bismuth telluride
CVD	chemical vapor deposition
EDS	energy-dispersive X-ray system
EELS	electron energy loss spectroscopy
FESEM	field emission scanning electron microscope
G	graphene
hBN	hexagonal boron nitride
HRTEM	high-resolution transmission electron microscope
QL	quintuple layer
SAED	selected area electron diffraction
SEM	scanning electron microscopy
Si	silicon
SiO ₂	silicon dioxide
STEM	scanning transmission electron microscopy
TEM	transmission electron microscope
TI	topological insulator
TMD	transition metal dichalcogenide

1 DEFENSE TECHNICAL
(PDF) INFORMATION CTR
DTIC OCA

1 CCDC ARL
(PDF) FCDD RLD CL
TECH LIB

1 GOVT PRINTG OFC
(PDF) A MALHOTRA

2 CCDC ARL
(PDF) FCDD RLW
SP KARNA
FCDD RLW MG
MH GRIEP